Suppression of NO_x emissions by intensive strain in lean premixed hydrogen flamelets

Porcarelli, Alessandro; Kruljević, Boris; Langella, Ivan

DOI
10.1016/j.ijhydene.2023.08.110

Publication date
2023

Document Version
Final published version

Published in
International Journal of Hydrogen Energy

Available online at www.sciencedirect.com

ScienceDirect

journal homepage: www.elsevier.com/locate/he

Suppression of NO_x emissions by intensive strain in lean premixed hydrogen flamelets

Alessandro Porcarelli[*], *Boris Kruljević*, *Ivan Langella*

Faculty of Aerospace Engineering, Delft University of Technology, Kluyverweg 1, Delft, 2629 HS, the Netherlands

HIGHLIGHTS

- NO_x formation is suppressed at high strain rates in lean premixed hydrogen-air flamelets.
- The redistribution of OH radicals at high strain rates is the main responsible for the suppression of NO_x formation.
- The mechanism of NO_x suppression is the same at atmospheric and higher pressure.
- The density-weighted integral NO_x emission has an almost linear dependence with the reciprocal of strain rate.

GRAPHICAL ABSTRACT

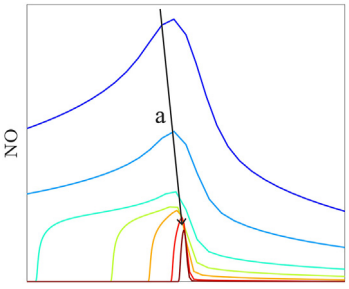

ARTICLE INFO

Article history:
Received 7 June 2023
Received in revised form
28 July 2023
Accepted 8 August 2023
Available online 04 September 2023

Keywords:
Strained flames
Hydrogen
Premixed combustion
CFD

ABSTRACT

NO_x formation in premixed, highly-strained, pure hydrogen-air flamelets is investigated at lean conditions. Detailed-chemistry, one-dimensional and two-dimensional simulations are performed on a reactants-to-products configuration with varying applied strain rate. The results highlight for the first time for lean pure-hydrogen flamelets that NO_x emissions are suppressed as strain rate is increased. The most substantial decrease is observed across the thermal NO_x formation pathway. Here the suppression of NO_x is triggered by a redistribution across the flamelet of the radicals involved in the pathway reactions. A comparison with methane flamelets is further performed to understand to what extent the observed trends with strain can be specifically linked to hydrogen burning features. Similar NO_x suppression trends with strain are also observed for increased pressure and different equivalence ratios, although with different rates of decrease. A correlation is proposed based on the observed results and further theoretical considerations, to predict NO_x emissions according to applied strain rate and equivalence ratio.

* Correponding author.
E-mail address: a.porcarelli@tudelft.nl (A. Porcarelli).

https://doi.org/10.1016/j.ijhydene.2023.08.110

Nomenclature

Δx	Horizontal grid spacing (mm)
Δy	Vertical grid spacing (mm)
$\dot{\omega}_c$	Progress variable reaction rate (kg/(m^3· s))
$\dot{\omega}_{NO}$	Mass rate of production of NO, or NO mass source term (kg/(m^3· s))
$\dot{w}$	Molar rate of production (mol/(cm^3· s))
φ	Equivalence ratio (–)
Φ_{NO}	Flux of NO across the outlet boundary (g/(cm · s))
ρ	Density (kg/m^3 or g/cm^3)
a	Applied strain rate (s^{-1})
c	Water-mass-fraction-based progress variable (–)
D	Diffusion coefficient (m^2/s)
h	Vertical domain dimension (m or cm) or specific absolute enthalpy (J/kg)
i	Index of direction
I_{NO}	Density-weighted NO integral (g/cm)
K	Local stretch rate (s^{-1})
k	Index of specie
$K_{f,r}$	Forward reaction coefficient of reaction r
$K_{r,r}$	Reverse reaction coefficient of reaction r
L	Horizontal domain dimension (m or cm)
ORR	Overall reaction rate (mol/(cm^2· s))
p	Pressure (bar or atm) or index of products domain boundary (unless differently specified)
q	Specific heat flux (J/kg)
r	Index of reactants domain boundary (unless differently specified)
T	Temperature (K)
u	Velocity (m/s)
V	Diffusion velocity (m/s)
X	Species mole fraction (–)
x	Flamelet longitudinal or normal coordinate (m or cm)
Y	Species mass fraction (–)
y	Flamelet vertical or tangential coordinate (m or cm)

1. Introduction

The yearly increasing energy demand is currently substantially met by fossil fuels, with consequent emissions of CO_2 and other pollutants. Renewable technologies have seen a strong growth in recent years and have been identified as one of the solution to satisfy this demand and reduce greenhouse emissions simultaneously. These technologies include solar PV, onshore and offshore wind, biofuels, and hydro [1]. However, direct electrification from renewable sources is not feasible for certain applications, such as aviation. Considering this scenario, hydrogen emerges as a promising alternative [2]. Hydrogen is carbon-free, and can be produced with electrolysis using renewable energy [3,4]. Hence, it can be either further converted to form methane [5], syngas [6], or ammonia [7], or used directly in fuel cells [8] or in combustion applications [9]. In the last decades, research efforts have focused on the possibility to burn hydrogen in lean premixed conditions, where the lower adiabatic flame temperature allows to decrease NO_x formation via the thermal route. Furthermore, hydrogen's strong reactivity and high lower-heating-value allow to reach ultra-lean conditions without necessarily incurring in lean blow-off. Earlier studies have discussed the influence of hydrogen addition on lean blow-off, showing that a minimal hydrogen enrichment can consistently decreases the blow-off equivalence ratio and thus broaden the possible burning regimes [10–13]. However, many technological challenges are involved with controlling hydrogen combustion in lean turbulent conditions. In fact, flashback and uncontrolled flame propagation that are typical of this regime [14,15] are amplified by the combination of hydrogen's high reactivity, implying also high flame speed [16], and its propensity to autoignite [17,18] and quickly diffuse [19].

One interesting property of hydrogen flames that has not been fully understood yet is its behaviour under intensive strain. The hydrogen-enhanced preferential diffusion effects and the strain sensitivity have been proved to be interdependent and to have a combined influence on the flame response [20,21]. For instance, for flames with fuel Lewis number below unity, increased strain rate has been correlated to an observed excess enthalpy relative to the undisturbed laminar flame, and thus to an increased flame speed [22]. Such flames have been also proved to align preferentially with extensive tangential strain levels in turbulent strained flames [23,24], and this particular characteristic can be potentially exploited in the design of novel combustor systems. For hydrogen-enriched laminar flames, previous studies have highlighted their peculiar performance with varying strain rates, further suggesting that high strain regimes can potentially be exploited for hydrogen combustion practical applications. Hydrogen addition has been shown to delay the extinction strain rate [10,11], proving that hydrogen is able to sustain very high strain rates. Furthermore, while the mass burning rate decreases with strain for pure methane flames, a certain amount of hydrogen addition inverts this trend, particularly in lean conditions [25]. Similar considerations hold for the peak heat release rate, which is found to increase with strain in lean hydrogen enriched flames [26]. The same trend has been also observed in a 2D direct numerical simulation of a turbulent strained hydrogen flame [24]. For syngas fuels, it was further shown that increasing the hydrogen percentage in the fuel at lean conditions affects the laminar flame response with strain in terms of flame temperature, NO_x emissions [27] and consumption speed [16]. However, the effect of these distinctive hydrogen burning features at high strain rates on NO_x for pure hydrogen-air lean premixed flames is still an open question.

From a broader point of view, the combined effect of flame strain and curvature, namely stretch, was shown to increase the consumption speed for lean enough conditions, which is opposite to what observed for hydrocarbon flames. This behaviour implies a change of sign in the Markstein length for a hydrogen case, which has been highlighted in both numerical [28] and experimental [29] studies of curved laminar spherical flames, and could be potentially exploited to increase the combustion efficiency in low NO_x lean regimes. Interestingly, Varea et al. [29] also observed super-adiabatic

products temperatures in relatively highly stretched flames. It is still unclear, however, whether the behaviours observed in the aforementioned studies with stretch would be observed by the sole effect of strain. Additional efforts are needed to understand the behaviour of highly strained flames, including their modelling at both laminar and turbulent condition, in order to characterize this yet unexplored flame regime.

In this study we numerically investigate counter-flow premixed laminar hydrogen flames to shed light on the behaviour under intensive levels of strain, in particular the effect on NO_x emissions. This is, to best of the authors' knowledge, the first time that such an investigation is conducted. The increase in heat release rate and the observation of super-adiabatic temperatures under stretched regimes discussed in the previous paragraphs would suggest a corresponding increase of NO_x emissions. Counter-intuitively, this study highlights that NO_x emissions do not increase with strain, and conversely they are suppressed at lean conditions, particularly at very high strain rates. Detailed-chemistry, high-fidelity one-dimensional and two-dimensional computational fluid dynamics (CFD) analyses are performed to achieve a deeper understanding of the employed counter-flow strained flamelet configuration for intensive strain levels. In particular, a detailed analysis of NO_x formation pathways shows that thermal NO_x mechanism is the main contributor to the pollutant decrease with strain. Hence, the way strain affects the main radicals distribution is investigated in order to shed light on the observed emissions pattern. The analysis is also repeated for a higher pressure level, different chemical mechanism, and several lean equivalence ratios to investigate the behaviour of NO_x under different conditions. The response of the hydrogen counter-flow flamelet is finally compared to that of a methane flame to highlight structural differences between fuels with different diffusivity and reactivity. A correlation is eventually proposed from the outcomes of these analyses, to predict the decay of the integral NO emissions with strain at different equivalence ratios. The physical behaviour of laminar flames investigated in this study is the first step to shed light on potential features of novel combustor systems, where NO_x emissions are controlled by stabilising the flame against intensive strain.

This paper is organised as follows. The governing equations used for the 1D and 2D cases are introduced in Section 2, followed by an overview of the numerical setups in Section 3. Emission results for hydrogen in atmospheric lean premixed conditions are then discussed in Section 4. First, a comparative analysis of emission trends with strain between 1D and 2D cases is performed (Section 4.1), after which NO_x formation pathways (Section 4.2) and radicals distribution in the flame (Section 4.3) are analysed. The emission behaviour under different conditions of fuel, pressure and equivalence ratio is discussed in sections 4.4, 4.5 and 4.6, respectively. The proposed correlation along with its derivation is presented in Section 5. Finally, conclusions are provided in Section 6.

2. Problem definition

2.1. *Strained flamelet configuration*

Strained flames can be commonly obtained using two canonical configurations documented in literature, which are reported in Fig. 1.

The first configuration is represented by a back-to-back or reactants-to-reactants counter-flow configuration, where two flames are stabilized symmetrically with respect to the flow stagnation plane (Fig. 1a). Several studies are available where the effects of hydrogen enrichment and strain on lean blow-off, extinction strain, mass burning rate, and NO_x emissions are investigated with this setup [10,11,25,27]. Specifically on NO_x emissions, a technical report from Xie and Wang [30] underlines a decreasing trend with strain for this configuration in rich pure-hydrogen flames, attributing to the NNH pathway the predominant contribution to NO_x formation at

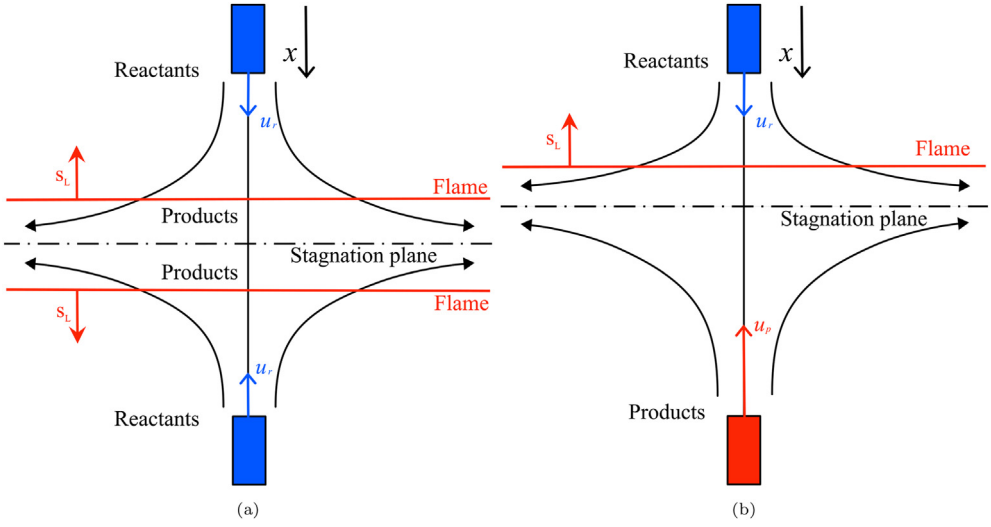

Fig. 1 – Sketch of the reactants-to-reactants or back-to-back (a) and reactants-to-products or fresh-to-burnt (b) counter-flow premixed strained flame configurations, where *x* is the flamelet longitudinal coordinate, u_r is the inlet velocity of the reactants mixture, u_p is the inlet velocity of the products mixture, and s_L is the laminar flame speed. Curved lines indicate the streamlines of the flow.

high strain levels. However, the limitation of this configuration is represented by the proximity of the two twin flames to each other, particularly at the high strain rates achievable by purely hydrogen flames. In these conditions, in fact, the combustion reactions have no space to complete, and this has been shown to have a negative impact on the prediction of the extinction strain rate [31,32]. Minor species are shown not be fully burnt within the stagnation plane in Figs. 5 and 6 of Jackson et al. [10]. Similarly, the reaction rates of NO_x pathways were observed to approach zero within the stagnation plane for lower strain rates in Ning et al. [27] (see Figs. 6-8 of their work), but not at higher strain rates. The same was observed to occur to the water rate of production in Xie and Wang [30] (see Figs. 2 of their work).

The second premixed strained flamelet configuration is represented by a reactants-to-products or fresh-to-burnt counter-flow, where a single flame stabilises on the reactants side of the domain (Fig. 1b). The single flame setup allows the combustion reactions to complete even at very high strain rates, as the fuel and the radicals have space to be burnt completely. This evidence can be found for instance in the work of Marzouk et al. [26], Figs. 4-6. Previous studies also proved that the extinction strain rate can be accurately predicted in this configuration [33]. On the other hand, the presence of complete combustion hot products on one of the boundaries can precondition the problem, particularly considering the products temperature.

Due to the discussed proximity of the two flames, the reactants-to-reactants configuration appears less suitable for investigations on emissions in highly-strained conditions. Therefore, the reactants-to-products configuration is employed in the present study, whose single flame layout allows the chemical reactions to complete also at very high strain rate. Despite the discussed possible preconditioning of the setup for the prescribed boundary conditions, the reactants-to-products configuration has been already employed for physical analysis of strained syngas and hydrogen-enriched laminar flames [16,26], and widely discussed for methane flamelets [34,35], particularly to compare flame speeds of turbulent cases with the strained flamelet speed [24,32] and in the application of LES-FGM models with strained flamelets [36,37]. Only this setup is thus carried on with the reminder of this paper.

2.2. 2D governing equations and numerical modelling

Both one-dimensional and two-dimensional simulations are performed. For the two-dimensional simulations, the reactingFoam transient compressible solver in OpenFOAM [38] is employed. The reacting Navier Stokes equations [39] are solved for mass, momentum, absolute enthalpy and N species with detailed chemistry. The equation for the generic specie k is

$$\frac{\partial(\rho Y_k)}{\partial t}+\frac{\partial(\rho u_i Y_k)}{\partial x_i}=-\frac{\partial(\rho V_{k,i} Y_k)}{\partial x_i}+W_k\dot{w}_k, \tag{1}$$

where subscripts i denotes direction i, W_k is the molar mass of the specie k, ρ is the mixture density, $V_{k,i}$ is the diffusion velocity vector, and $\dot{w}_k$ is the molar rate of production of species k. Radiation, body forces, and viscous dissipation effects are neglected. The Dufour effect on the heat flux is also neglected for simplicity.

The ideal gas law and the caloric equation of state are used as thermodynamic model, where the species heat capacities are obtained using the JANAF polynomials. Given the lean conditions investigated in the present work, the mixture viscosity is computed with Sutherland's law with the properties of air for simplicity. The mixture conductivity is found from the viscosity with the modified Eucken correlation [40]. Only laminar conditions are considered in this study, while the effect of the turbulence-chemistry interaction will be investigated in a future study. A mixture-averaged diffusion model [39] is used to model the diffusion velocity and account for the low Lewis number of the hydrogen fuel as follows:

$$V_{k,i}=-\frac{D_k^M}{X_k}\frac{\partial X_k}{\partial x_i}\approx\frac{D_k^M}{Y_k}\frac{\partial Y_k}{\partial x_i} \tag{2a}$$

$$D_k^M=\frac{1-Y_k}{\sum_{l,k\neq l}^{N}X_l/D_{kl}} \tag{2b}$$

The binary diffusion coefficients D_{kl} for the species involved in the reactions are found with the Chapman-Enskog correlation [41,42]. To avoid the system over-determination, the mass fraction of the most abundant species (N_2) is found as $Y_N=1-\sum_{k=1}^{N-1}Y_k$ instead of solving its transport equation.

Detailed kinetic data of reactions from GRI-3.0 mechanism [43] are used to obtain consumption and production rate of species. Generally taken as a reference scheme for methane [44], a recent study by Cazeres [45] considered GRI-3.0 as the starting detailed scheme for the generation of reduced mechanisms for the combustion of hydrogen and methane-hydrogen blends. His analysis showed that optimized reductions of GRI-3.0 provide accurate predictions of the burning parameters of these fuels under a broad range of regimes, ultimately concluding that hydrogen combustion chemistry is contained in methane-air combustion schemes. In light of this conclusion, in order to reduce the CPU time, the GRI-3.0 mechanism has been reduced in this study removing all the carbon species and the related reactions. Furthermore, while previous studies highlighted the limitations of the scheme in the prompt NO_x prediction [46,47], in this study pure hydrogen is considered as fuel and thus no carbon species enabling the formation across this pathway are present. In order to further speed up the simulations, the TDACChemistryModel in OpenFOAM is also adopted, consisting of the combination of the *in situ* adaptive tabulation (ISAT) algorithm with the dynamic adaptive chemistry (DAC) reduction scheme [48].

2.3. 1D governing equations and numerical modelling

One-dimensional simulations are run with CHEM1D [49], which is a widely-validated code for one-dimensional flame simulations [25]. In one dimension and for a planar reactants-to-products counter-flow flame, the set of conservation equations solved in CHEM1D is expressed as follows [50]:

$$\frac{\partial \rho}{\partial t} + \frac{\partial (\rho u_x)}{\partial x} = -\rho K \tag{3a}$$

$$\frac{\partial (\rho Y_k)}{\partial t} + \frac{\partial (\rho u_x Y_k)}{\partial x} = -\frac{\partial (\rho V_{x,k} Y_k)}{\partial x} + W_k \dot{\omega}_k - \rho K Y_k \tag{3b}$$

$$\frac{\partial \rho K}{\partial t} + \rho u_x \frac{\partial K}{\partial x} = \frac{\partial}{\partial x}\left(\mu \frac{\partial K}{\partial x}\right) + \rho_p a^2 - \rho K^2 \tag{3c}$$

$$\frac{\partial \rho h}{\partial t} + \frac{\partial \rho u_x h}{\partial x} = \frac{\partial q}{\partial x} - \rho K h \tag{3d}$$

where the density of the products mixture ρ_p, the applied strain rate a, the local stretch rate K, the specific absolute enthalpy h and the specific heat flux q, have been introduced. The system is again closed with the caloric equation of state and the ideal gas low, where in the latter a low Mach-number approximation is introduced. The applied strain rate a is a setup parameter and is defined as the velocity gradient at the products boundary:

$$a = -\left(\frac{du_x}{dx}\right)_p. \tag{4}$$

The influence of the y-component (flame-tangential) of the flow on the transport of scalars is taken into account with the introduction of the local stretch rate [50]:

$$K(x) = \frac{\partial u_y}{\partial y}. \tag{5}$$

As a consequence of the continuity equation, the relation between the two parameters above reads $K_{x\to\infty} = a$. The GRI3.0 is used as chemical mechanism, along with a mixture-averaged diffusion model (Eq. (2.2)). Empirical laws are used for viscosity and conductivity in CHEM1D, and the binary diffusion coefficients are computed using molecular potentials and are tabulated as a function of temperature in polynomial form. The reader can find further details in [51].

3. Computational setup

The combustion of hydrogen is evaluated at atmospheric conditions and at 5 bar. Temperature and species boundary conditions at the reactants and products boundary are prescribed as follows for both 1D and 2D cases. An equivalence ratio of $\varphi = 0.7$ is imposed for both streams. The reactants temperature is $T_r = 300$ K, while the products temperature is set to the adiabatic flame temperature of an unstrained hydrogen flamelet with the same equivalence ratio computed with CHEM1D, $T_p = 2021$ K. Mass fractions at the products boundary are imposed from complete combustion. A summary of the temperature and species boundary conditions for both 1D and 2D simulations are reported in Table 1.

Table 1 – Temperature and species boundary conditions for 1D and 2D simulations, for a hydrogen flame at $p = 1$ atm and $\varphi = 0.7$.

Quantity	Left boundary (reactants)	Right boundary (products)
T [K]	300	2021
Y_{H_2} [–]	0.02	0
Y_{O_2} [–]	0.228	0.068
Y_{H_2O} [–]	0	0.18
Y_{N_2} [–]	0.752	0.752

3.1. 1D setup

For the one-dimensional simulations, a relatively wide computational domain of $L_{1D} = 20$ cm is chosen, where L is the length in the streamwise direction. CHEM1D uses an adaptive mesh algorithm, thus ensuring a sufficiently accurate mesh refinement in the flame region. The adaptive grid accounts for 200 points in total. An exponential differential scheme is used for the spatial discretization, and a second-order time integration of the differential equations is performed by the stationary solver. The time step is adjusted automatically by the numerical tool to achieve convergence, and ranges between 10^{-6} s and 10^{-8} s. The only input parameter for the velocity field is represented by the applied strain rate a, defined in Eq. (4). According to the applied strain rate definition, the higher is a, the higher will be the boundary velocity and the stretch rate experienced by the flame. Also, the velocity field is solved such that the stagnation plane is always found at the center of the domain, i.e. fulfilling the $u(x = 0) = 0$ condition. Hence, the boundary velocities are determined by the solver for each strain rate depending on the chosen domain extension at both sides, where the domain extension is irrelevant to the flamelet calculation, provided that the flame is stabilized within the domain and sufficiently far from the boundaries. A broad range of applied strain rates is investigated for 1D simulations, from 100 s^{-1} up to 20000 s^{-1}. Although these levels of strain are significantly above the extinction strain rate found for methane-air flames (about 2000 s^{-1} at stoichiometric conditions [52]), only near the high side of the above range the hydrogen flames start to exhibit signs of extinctions. The one-dimensional flames are relatively quick to compute, with computational time ranging from few minutes to few hours depending on the applied strain rate.

3.2. 2D setup

Two-dimensional laminar simulations are performed to enhance the physical understanding of the 1D results, and ultimately to verify the NO_x emission behaviour with strain observed in the 1D simulations. For this reason, only two representative, relatively-high applied strain rates configurations are investigated in the 2D case, $a = 2000$ s^{-1} and $a = 5000$ s^{-1}. Although experimental data at such strain levels is not available in the literature for validation purposes, these two-dimensional simulations are essential to extract further information on the behaviour observed for the one-dimensional cases, and allow to identify possible multi-directional effects that could not be observed in the flamelets. An implicit second-order Euler-backward discretization scheme for time marching is used for the 2D simulations, along with a second-order central scheme for the convective term of all resolved quantities. Since OpenFOAM is a finite volume solver and does not offer high-order polynomial schemes, the simulation performed are categorized here as laminar quasi-DNS. For a reacting flow test case, Zirwes et al.

[53] showed that a flame-resolved quasi-DNS solution with a cubic discretization scheme compares to experimental data within a 1% error. Their study also showed that quasi-DNS simulations of canonical flows with second order central schemes well match the solutions from higher-order finite differences DNS codes, with an error of 5–10%. This range of error is acceptable for the purpose of the present 2D analysis of validating the NO_x emissions trends observed in 1D. A variable time step is used ensuring a maximum Courant number of 0.5 for all domain. The simulations are run for a physical time of $t = 0.5$ s for both the applied strain rates investigated, corresponding to more than 100 times the maximum estimated flow-through time inside the domain. A typical computation required 225 and 895 CPU-hours respectively for lower and higher strain rate cases.

The higher computational cost of two-dimensional quasi-DNS simulations led to the choice of decreasing the dimension of the domain to $L_{2D} = 2$ cm in both the horizontal and the vertical directions. Nevertheless, this size was sufficient to fully enclose the flame within the domain and ensure a flame position far enough from the boundary for all simulations. The mesh consists of 100 uniform quadrilaterals in the x-direction and 40 in the y-direction, resulting into a cell spacing of $\Delta x = 0.2$ mm and $\Delta y = 0.5$ mm respectively for the streamwise and flame-tangential directions. The mesh is refined progressively by a factor of 2 for three times in the proximity of the flame. An example for $a = 5000$ s^{-1} is provided in Fig. 2, and a more comprehensive mesh independence analysis can be found in the supplementary material, Section 1.

The flame position is determined for every applied strain rate combining preliminary coarse 2D simulations and 1D simulations. The use of a central difference scheme also allows to benefit of additional numerical dissipation that stabilises the solution in the mesh refinement interfaces, where numerical instabilities may arise. Unlike in CHEM1D, where the applied strain rate a was the only input parameter for the velocity field, a uniform velocity at the two inlets is prescribed for the 2D simulations. The values assigned for the axial velocity at the reactants and products boundaries (indicated respectively by the subscripts 'r' and 'p') are extracted from the 1D simulations, i.e.

$$u_{r,2D} = (u_{1D}(x = -1\ \text{cm}))_{a=\text{const}}, \tag{6a}$$

$$u_{p,2D} = (u_{1D}(x = 1\ \text{cm}))_{a=\text{const}}. \tag{6b}$$

These values are reported in Table 2.

A zero gradient boundary condition is assigned at the upper and lower boundaries. Note that, since the assignment of velocity profiles in the 2D cases does not also imply constant strain rate at the boundary, some discrepancy is expected in the solution along the centreline between 1D and 2D cases. Nevertheless, these differences do not affect the generalities of the analyses to be conducted next.

4. Results

4.1. NO_x emissions trends

NO_2 mass fraction peaks were shown to be at least three orders of magnitude smaller than the ones of NO for any of the setups investigated. Therefore, similarly to previous studies [27], NO emissions will be considered representative of the overall NO_x emissions. The behaviour of Y_{NO} across a hydrogen-air flamelet at an equivalence ratio $\varphi = 0.7$, and for different applied strain rates, is shown in Fig. 3a. It is immediately observable that both the peak and the area under the curves of NO mass fraction decrease significantly as the applied strain is

Table 2 – Inlet velocity boundary conditions assigned at the reactants ($u_{r,2D}$) and products ($u_{p,2D}$) side of two-dimensional simulations for the two values of applied strain rate a.

a [s^{-1}]	$u_{r,2D}$ [m/s]	$u_{p,2D}$ [m/s]
2000	5.31	−21.85
5000	16.84	−53.92

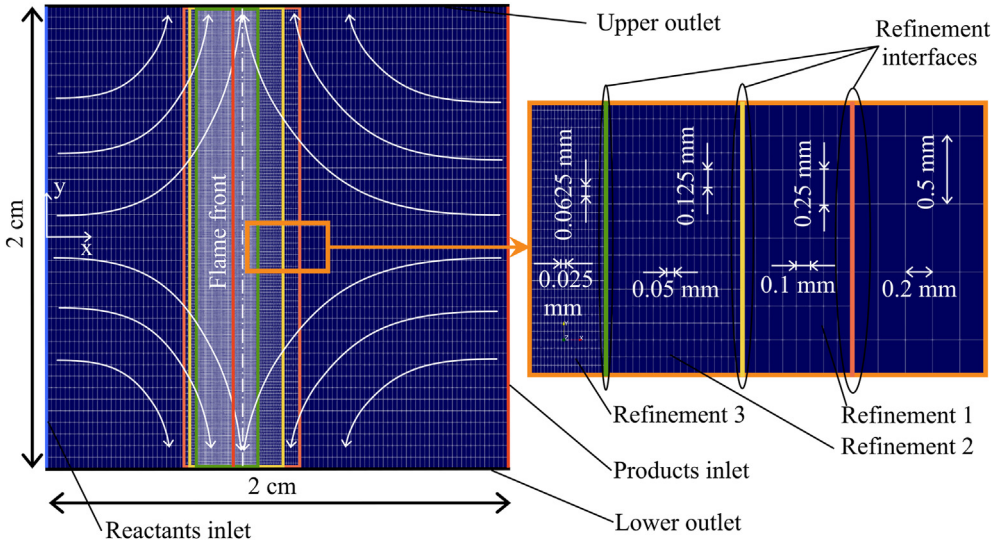

Fig. 2 – Sketch of the two-dimensional setup with mesh refinement for $a = 5000$ s^{-1}.

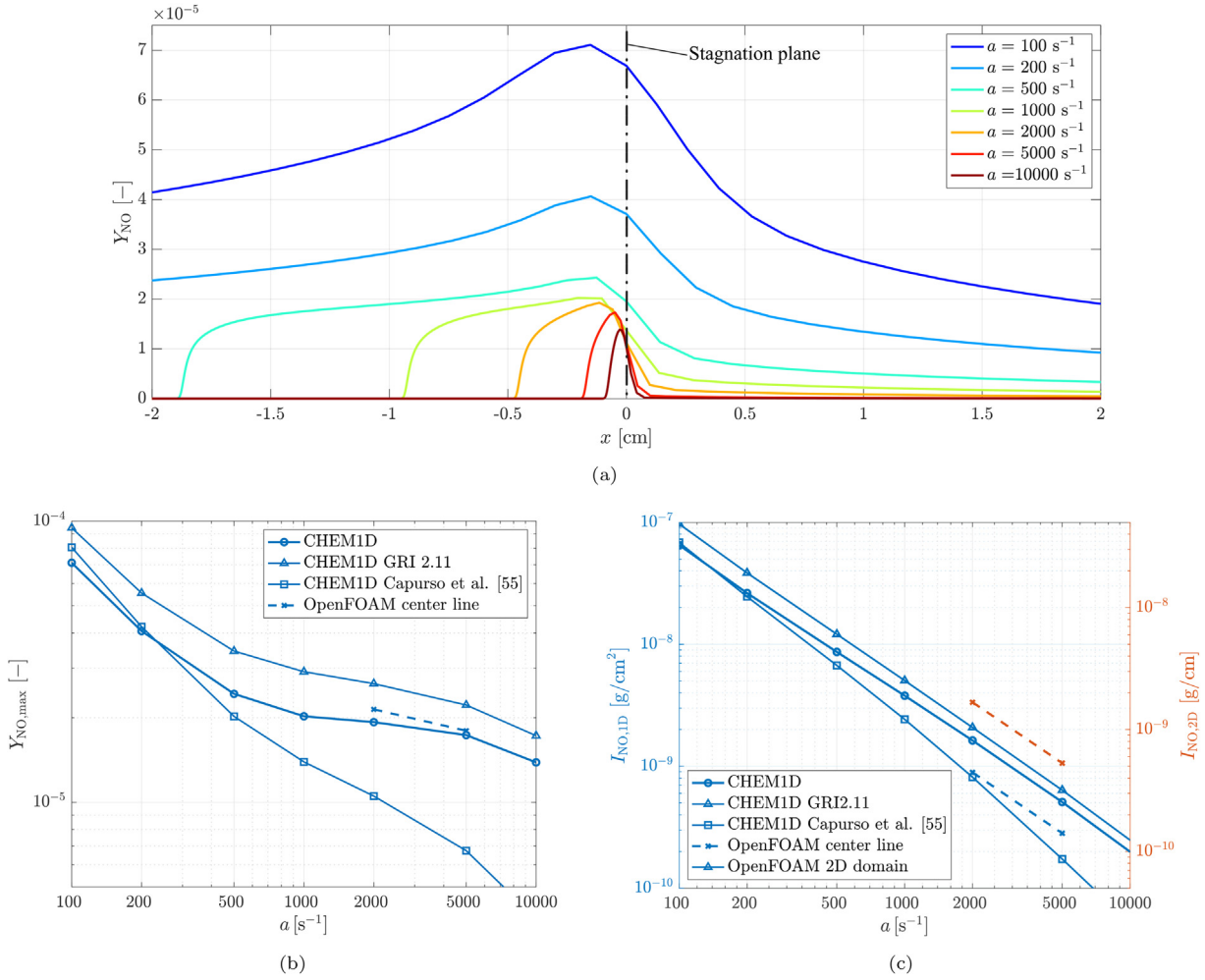

Fig. 3 – (a) NO mass fraction (Y_{NO}) across the longitudinal coordinate x in a one-dimensional hydrogen-air flamelet at equivalence ratio $\varphi = 0.7$, for different applied strain rates a. Variation of peak NO mass fraction $Y_{NO,max}$ (b) and density weighted NO integral $I_{NO,1D}$ (c) with strain rate for 1D and 2D simulations of hydrogen-air flames at equivalence ratio $\varphi = 0.7$. Wherever the chemical mechanism is not specified in the legend, GRI-3.0 is used.

increased, up to a factor of about 5 if one compares the highest ($a = 100\ s^{-1}$) and lowest ($a = 10000\ s^{-1}$) peaks. It is worth to note that no extinction is observed at the highest strain rates achieved, indicating that pure hydrogen-air flames can sustain very high strain levels, in line with observations in previous studies [10,11]. Furthermore, as strain increases, the peak value of NO decreases in relative percentage less, e.g. the relative decrease between $a = 5000\ s^{-1}$ and $a = 10000\ s^{-1}$ is only about 20%. This however does not imply that the overall suppression of NO also reaches a plateau as strain increases, and in fact NO decreases almost linearly (in the logarithmic space) instead, as will be discussed later.

In Fig. 3b the decrease of the peaks of Y_{NO} in the one-dimensional case, and along the centreline for the two-dimensional simulations, is further highlighted. The differences observed between 1D and 2D results at the same applied strain are the consequence of the different boundary conditions as discussed in Section 3.2. As observed in the figure, the suppression of NO peak with strain is confirmed in the 2D case. In order to have an understanding of the overall behaviour of NO in the domain, the density-weighted NO integral is also shown in Fig. 3c (refer to the left y-axis), where the integral is calculated as

$$I_{NO,1D} = \int_{-L/2}^{L/2} \rho Y_{NO} dx. \tag{7}$$

As observed in the figure, the integral amount of NO decreases almost linearly in the logarithmic space with strain, indicating that strain remains as effective in suppressing NO_x also at very high values. Further curves are shown in Fig. 3 where two additional chemical mechanisms are used in place of the GRI-3.0 in order to evaluate the effect on the prediction of NO. GRI-2.11 is tested in light of previous studies where it provided generally improved estimations of NO emission [44,54], along with the recently-published mechanism from Capurso et al. [55]. While different, albeit within the same order of magnitude, quantitative values are observed, particularly at higher strain rates for the Capurso et al. [55] scheme, the NO decreasing trend is maintained, suggesting that the choice of the mechanism does not affect the generalities of the results presented in this study. Nevertheless,

results suggest that the mechanism has to be chosen with care if one aims to obtain quantitative estimations.

One might argue that NO is a slow species which would form downstream of the flame in the hot products region, and this formation in the products side is prevented by the right boundary condition, where $Y_{NO}(x = L/2) = 0$ is imposed. In fact, in the present configuration Y_{NO} peaks near the stagnation plane to then rapidly drop to fulfill the boundary condition, see Fig. 3a. On the other hand, the investigation of the 2D simulations, where the NO is free to form in the y-direction (tangential to the flame in Fig. 1), suggests this not to be the case, i.e. NO is suppressed at high strain by some other means. Hence, the focus is shifted to the understanding of the emission behaviour in the flame-tangential direction of the two-dimensional simulations. One can compute for this purpose the two-dimensional density-weighted NO integral for the 2D setups by integrating on the 2D-domain surface as follows:

$$I_{NO,2D} = \int_A \rho Y_{NO} dA. \tag{8}$$

This integral is also reported in Fig. 3c (refer to the right y-axis). As one can observe, the suppression of NO with strain seems to follow the same linear trend in the logarithmic space as that observed for the 1D simulations. From the analysis of the 2D data it is further observed that

$$I_{NO,2D} \approx I_{NO,1D} \cdot L_{2D}, \tag{9}$$

i.e. the 1D integral of NO calculated across the centreline of the 2D solution, multiplied by the vertical dimension, is approximately equal to the 2D integral. These considerations raise confidence on the fact that the suppression of NO_x observed in 1D simulations and in the 2D domain centreline as strain is increased is not compensated by any additional NO formation in the vertical direction. Further evidence on this can be provided by following the NO formation along the same streamline at the two different strain rates investigated for the 2D cases. This is shown in Fig. 4, where a streamline intersecting the reactants boundary at a vertical position $y = -0.2$ mm is shown. This streamline is chosen such that it crosses the flame, continues in the products stream, and exits the domain without intersecting the stagnation plane. The residence time of a parcel of fluids travelling along this streamline for the case at $a = 5000\ s^{-1}$ is about $\Delta t = 1.23$ ms. During the same time, a parcel of fluids in the reactants entering the domain for the case at $a = 2000\ s^{-1}$ at the same vertical position as the $a = 5000\ s^{-1}$ case, has travelled less distance, as indicated by the pathline shown for this case in Fig. 4b, and ends up positioned upstream the flame at a relative vertical position $y = -0.53$ mm from the centreline. The integral amount of NO is at this point computed across the flame (streamwise direction) at the section crossing this position, and compared to that evaluated at the exit section for the higher strain (see green lines in Fig. 4). These values of integral NO are provided in Table 3.

By investigating this data one can notice that not only the NO integral is lower for the higher strain rates (despite it is computed at a section where it had the same time to form as for the lower strain rate case), but also that the values of integral NO for the two cases are very close to the ones along the centreline reported in the graph in Fig. 3c. This indicates that there is no additional NO formation in the vertical direction at higher strain rates, and thus the suppression of NO_x at increased strain is not a mere consequence of the decreased residence time. For comparative purposes the flux of NO across the outlet boundary is also shown in Table 4 for the two strain rates. This flux is defined as

Table 3 – Density-weighted NO integral values across the sections in green indicated in Fig. 4, for two different applied strain rates *a*.

a [s^{-1}]	y(Δy) [mm]	I_{NO}(y) [g/cm^2]
2000	−0.53	$8.39 \cdot 10^{-10}$
5000	−10	$2.82 \cdot 10^{-10}$

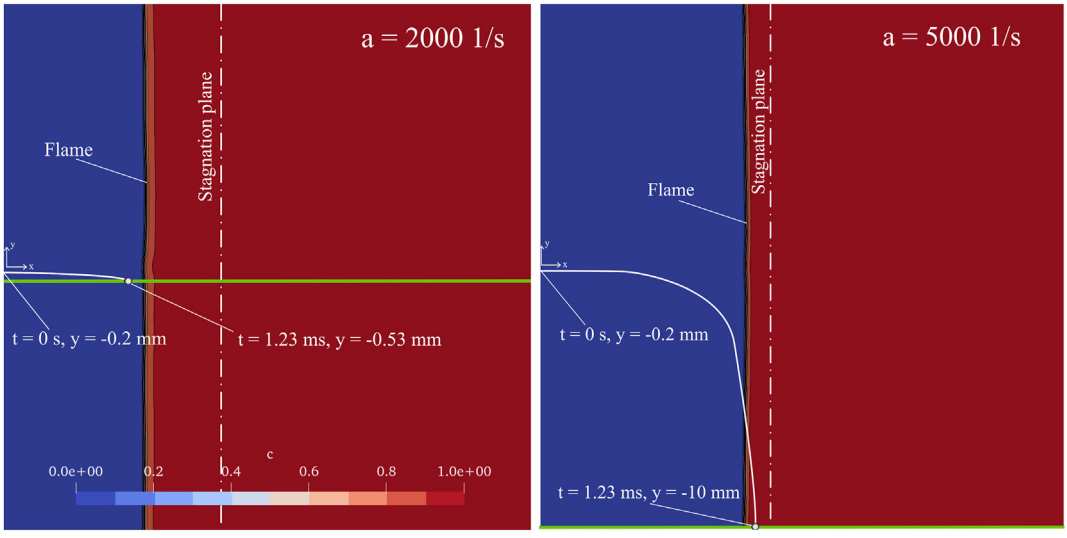

(a) $a = 2000\ s^{-1}$. (b) $a = 5000\ s^{-1}$.

Fig. 4 – Streamlines intersecting the left boundary at vertical coordinate $y = -0.2$ mm for two applied strain rates *a* are plotted on top of water mass fraction based normalised progress variable contours. Green lines indicate the section along with the integral of NO is computed for the two cases after the same travelling time $t = 1.23$ ms.

Table 4 – Flux of NO (per unit width) across the lower outlet surface (refer to Fig. 2) at two different applied strain rates *a*.

a [s^{-1}]	y [mm]	$\Phi_{NO}(y)$ [g/(cm·s)]
2000	−10	$2.48 \cdot 10^{-4}$
5000	−10	$1.90 \cdot 10^{-4}$

$$\Phi_{NO} = \int_{-L/2}^{L/2} \rho u_y Y_{NO} dx, \tag{10}$$

While the increased outlet speed for the higher strain rate case (due to the increased inlet speed) implies also an increase in the total mass flux, a decreased value in the NO flux is still observed for the higher strain rate, which gives further evidence that the decreased residence time at the higher strain rate is not by itself the reason behind the observed suppression of NO_x.

According to the above analyses the observed NO_x suppression with increasing strain is neither a consequence of the specific counter-flow configuration and boundary conditions, nor of the decreased resident time of the fluid particles in the domain. The suppression of NO_x must thus be associated to a direct effect of the increased tangential velocity gradients on the hydrogen flame combustion. This will be further investigated in the next section by analysing the NO formation pathways.

4.2. *NO formation pathways*

The focus is now shifted to the evaluation of the NO formation pathways, with the goal of further understanding the physical reasons behind the observed NO decrease with strain. As carbon species are not involved in hydrogen combustion, the prompt NO_x formation pathway is not considered, and the only pathways evaluated are thermal NO, NNH–NO, NNH–HNO–NO and N_2O–NO. CHEM1D solutions data are used for the purposes of the present NO formation routes investigations, since the NO emissions behaviour with strain was observed to be the same for the two-dimensional simulations (see Fig. 3c). Two high applied strain rates setups of $a = 2000\ s^{-1}$ and $a = 5000\ s^{-1}$ are analysed. For a sample reaction r involved in a pathway $\nu_A A + \nu_B B \leftrightarrow \nu_C C + \nu_D D$, the forward, $K_{f,r}$, and backward, $K_{r,r}$, reaction coefficients are obtained using the Arrenhius law as [39]:

$$K_{f,r}(T) = A_r T^{\beta_r} e^{\left(\frac{-E_{a,r}}{R_0 T}\right)}, K_{r,r}(T) = \frac{K_{f,r}}{\left(\frac{p_a}{R_0 T}\right)^{\sum_s \nu_s} e^{\left(\frac{\Delta S_r^0}{R_0} - \frac{\Delta H_r^0}{R_0 T}\right)}}, \tag{11}$$

where A_r, β_r and $E_{a,r}$ are found in the GRI3.0 mechanism reaction web page [43], and ΔS_r^0 and ΔH_r^0 are respectively the reaction entropy and enthalpy that can be found as a function of temperature with JANAF polynomials. The respective forward and reverse reaction rates are found as

$$\dot{w}_{f,r} = K_{f,r}(x) \cdot [A(x)]^{\nu_A} [B(x)]^{\nu_B}, \dot{w}_{r,r} = K_{r,r}(x) \cdot [C(x)]^{\nu_C} [D(x)]^{\nu_D}. \tag{12}$$

where the quantities in square brackets indicate the concentration of the species. Three-body and pressure-dependent reactions have been treated with dedicated formulas [56]. Following the formulation of Ning et al. [27], the overall reaction rate (ORR) of the reaction r is obtained by integrating the net reaction rate across the longitudinal (flame-normal) direction:

$$ORR_r = \int_{-L/2}^{L/2} \dot{w}_r(x) dx. \tag{13}$$

Summing the contribution of the ORR for the single reactions along a specific route, a chart diagram indicating the NO formation pathways at $a = 2000\ s^{-1}$ and $a = 5000\ s^{-1}$ is obtained, which is shown in Fig. 5a for the two strain rates.

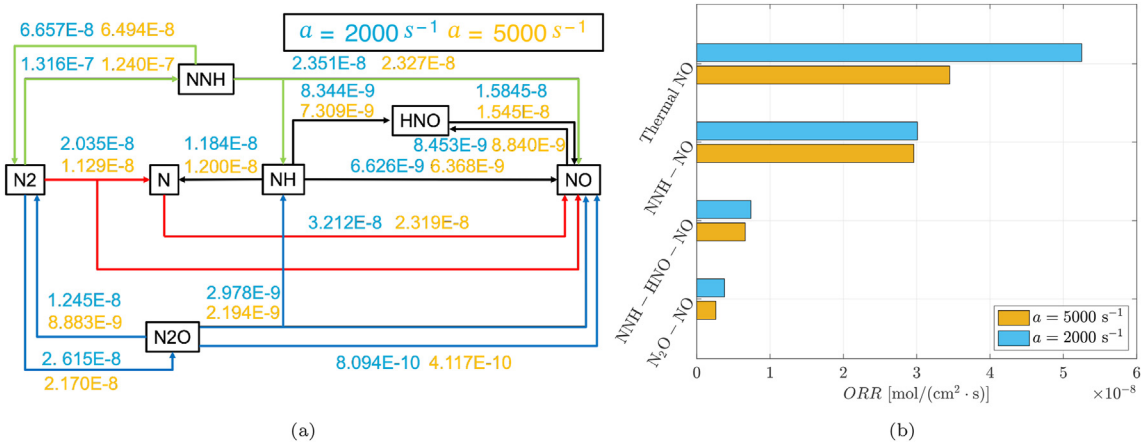

(a) (b)

Fig. 5 – (a) Chart diagram showing the overall reaction rates (in mol/(cm²·s)) over each specific reaction route along the NO formation pathways for a hydrogen-air flamelet, and for strain levels $a = 2000\ s^{-1}$ (light blue values) and $a = 5000\ s^{-1}$ (yellow values). Thermal NO pathway is highlighted in red, NNH–NO pathway in green, NNH–NO–HNO intermediate pathway in black, and N_2O–NO pathway in blue. (b) Contribution of each NO formation pathway to the total NO formation for strain levels $a = 2000\ s^{-1}$ (light blue) and $a = 5000\ s^{-1}$ (yellow).

While all the reaction rates involved in the pathways are observed to decrease in magnitude at higher strain, one can notice that this decrease is stronger for the thermal NO pathway. For instance, the highest reduction of NO between the two different strain rates of 45% is observed for the rate of decomposition of N_2 into N. Since the formation of N is what enables the formation of NO across the thermal pathway, this observation suggests that this pathway is the main responsible for the overall NO_x suppression with strain, as highlighted in Section 4.1. To further investigate on this, the ORR of the reactions directly producing NO in each pathway is also summed, and the resulting values are presented in the bar chart in Fig. 5b. The graph shows that the main NO production pathways for a lean hydrogen strained flame are both the thermal and the NNH. Moreover, the histogram confirms that the strongest decrease of NO production at high strain rates is associated to the thermal pathway. One could generally expect this to just be the outcome of a decreased flame temperature with increasing strain rate [57]. Nevertheless, for the flames investigated in the present work, increasing superadiabatic temperatures are observed as strain is increased (see Section 2 in the supplementary material), which is in line with previous studies for strained syngas [16] and spherical pure-hydrogen flames [29]. Hence, the reason behind the observed NO suppression is not imputable to a change in the flame temperature despite the dominant mechanism being the thermal one. The behaviour of radicals is thus investigated next to shed light on the reasons of the observed NO_x suppression.

4.3. *Analysis of radicals*

The investigation in Section 4.2 suggests that a more extensive analysis should be performed on the concentration of the radicals involved in the pathway reactions in order to further shed light on the physical explanation behind the phenomenon of NO_x suppression with strain in lean premixed hydrogen flames. Fig. 6a-d shows the distribution of the main radicals participating in the hydrogen-air combustion process as a function of the flame-centered, flame-thickness-normalised longitudinal coordinate, for a range of applied strain rates between $a = 100\ s^{-1}$ and $a = 10000\ s^{-1}$. The flame position at different strain rates is defined as $x_0 = x(c = 0.5)$, where the progress variable c is based on Y_{H_2O} and is normalised to vary between 0 and 1. The thermal thickness δ is taken as flame thickness, and its values at the different strain rates are reported in Table 5.

For all the radicals except atomic oxygen, the peak of their respective mass fractions is observed to increase with strain. As suggested in previous studies [26,55], particularly considering the H radical, this phenomenon is the responsible for the increase of the peak heat release rate and reaction rate with strain. This behaviour is also reported in the supplementary material for clarity, in Section 3, using results of the present study and the reaction rate of progress variable, $\dot{\omega}_c$. It is interesting to observe from Fig. 6 that all the main radicals are consumed immediately downstream of the flame at higher strain rates, which results in lower values of mass fractions downstream of the flame as compared to the cases at lower strain. This is likely due to the stronger convection that characterises the highly-strained regimes, that 'pushes' the radicals towards the flame, limiting their diffusion downstream in the hot products.

In Fig. 6f, the distribution in space of the mass source term of NO, $\dot{\omega}_{NO}$, at different strain rates is further shown. This quantity is observed to vary with strain, consistently with the variation of radicals involved in NO formation highlighted in the previous paragraph. In fact, while a local increase of NO formation with strain is observed in the proximity of the flame, i.e. in at the location where the peaks of the radicals are found (in particular of H and N), an opposite trend is found more downstream in the hot products region. Since an increased H concentration is known to promote the oxidation of N_2 to NNH [55,58], the corresponding local increase with strain of $\dot{\omega}_{NO}$ can be attributed to an enhanced NO formation through the NNH pathway. This consideration is supported by Fig. 6e, where the peaks of NNH mass fraction is shown to increase accordingly with increasing strain rate. In contrast, the lower availability of radicals at higher strain rates downstream of the flame is probably the main responsible factor determining the decrease of thermal NO formation with strain, observed in Section 4.2. In order to better understand this behaviour, the rate of the three reactions involved in the thermal NO route are plotted as a function of space across the flamelet for two different strain rates ($a = 2000\ s^{-1}$ and $a = 5000\ s^{-1}$) in Fig. 7.

Once again, higher peaks of reaction rates are observed at higher strain rates. In particular, the rate increase of the first reaction (blue lines in Fig. 7) seems to be contributing to the local increase of N concentration observed in Fig. 6b. On the other hand, the rate of the three reactions drops at higher strain at more downstream positions. Considering again the first of the reactions indicated in the figure, less N radicals are formed where $(x - x_0)/\delta > 5$, probably because of a decreased availability of reaction-enabling radicals of atomic oxygen, which is observable in Fig. 6d. As a consequence, the rates of the second and the third reactions indicated in the figure are limited in this region as well by the lower availability of N radicals. Furthermore, the rate of the third reaction indicated in the figure is also limited by the locally lower OH availability at higher strain highlighted in Fig. 6a. It can thus be concluded that the amount of O and OH radicals has a direct influence on the rate of NO formation via the thermal route, which is consistent with past experimental studies [58,59]. Overall, the downstream decrease of the rate of the reactions involved in the NO formation via thermal route at higher strain is the responsible of the observed local decrease of the total NO source term, shown in Fig. 6f. In light of the overall decrease of NO emissions with strain highlighted in Section 4.1, it can be

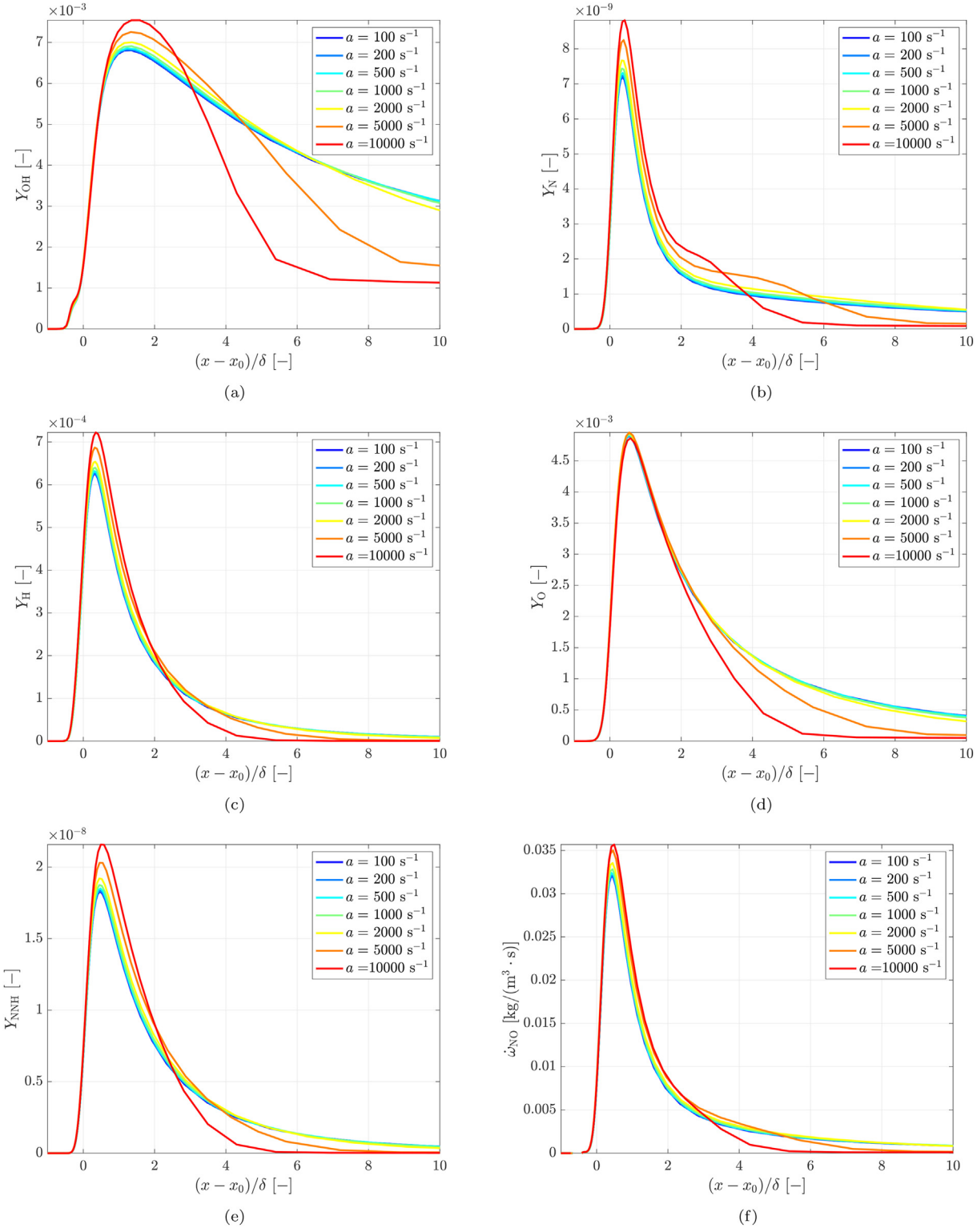

Fig. 6 – Distribution of OH (a), N (b), H (c), O (d), and NNH (e) radicals mass fraction Y_k across a hydrogen-air flamelet at equivalence ratio $\varphi = 0.7$ and for different strain rates a. The NO source term $\dot{\omega}_{NO}$ is also shown (f).

Table 5 – Thermal thickness δ in a hydrogen-air flamelet at equivalence ratio $\varphi = 0.7$ and for different strain rates a.

a [s^{-1}]	100	200	500	1000	2000	5000	10000
δ [mm]	0.330	0.330	0.329	0.328	0.324	0.312	0.294

further concluded that the discussed decrease of NO formation rate at more downstream positions overcompensates for the local increase observed closer to the flame, and is itself the responsible for the overall lower emissions of NO at high strain.

4.4. Comparison with methane

In the following section, we analyze methane-air flamelets to investigate how specific characteristics of hydrogen's combustion, including both its high diffusivity and increased reactivity caused by chain-branching consumption, contribute to the observed reduction in NO_x emissions. In Fig. 8a, the density weighted NO integral as a function of strain is plotted for two different methane-air flamelets at two different equivalence ratios. All other parameters are the same as those used for the hydrogen-air case discussed in the previous sections.

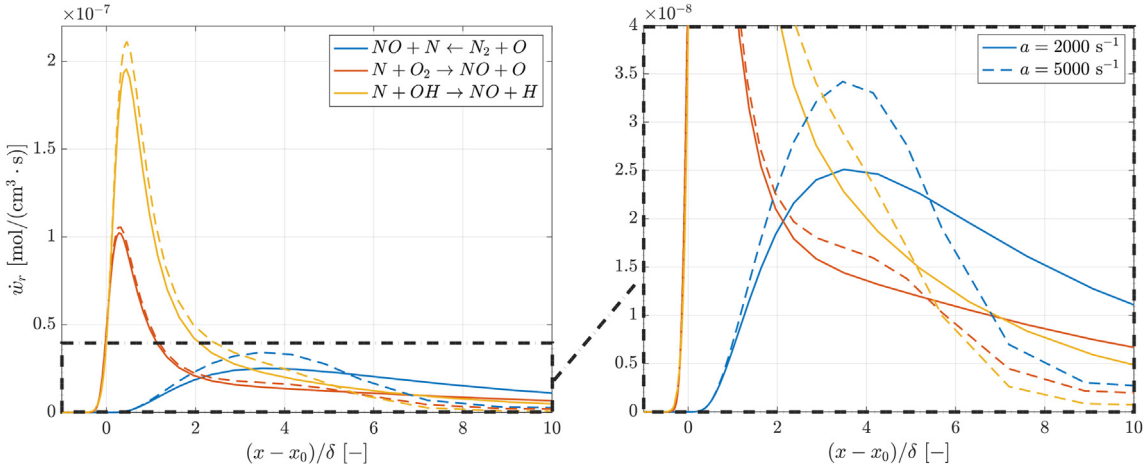

Fig. 7 – Molar rate of thermal NO_x reactions $\dot{w}_r$ across a hydrogen-air flamelet at equivalence ratio $\varphi = 0.7$, for two applied strain rates of $a = 2000$ s^{-1} (solid line) and $a = 5000$ s^{-1} (dashed line). A zoom in the region indicated by the dashed rectangular area is shown on the right for clarity.

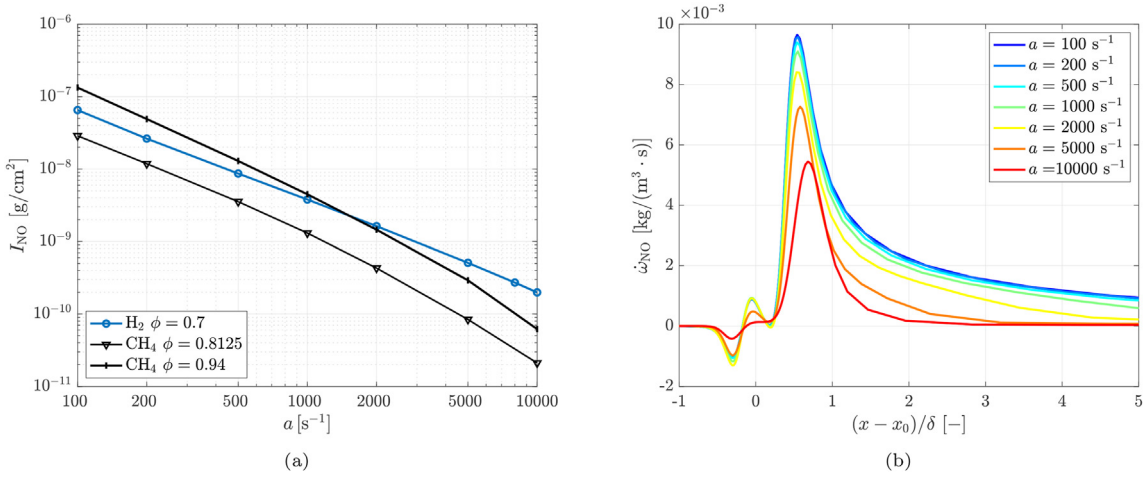

Fig. 8 – (a) Variation of density weighted NO integral I_{NO} with strain a for a methane-air flamelets at two equivalence ratios and hydrogen-air flamelet at $\varphi = 0.7$. (b) NO source term $\dot{\omega}_{NO}$ across the flamelet for different strain rates for methane at $\varphi = 0.8125$ (same adiabatic flame temperature as hydrogen at $\varphi = 0.7$).

The first equivalence ratio, $\varphi = 0.8125$, is chosen such that the same adiabatic flame temperature of hydrogen at $\varphi = 0.7$ is achieved in the products, $T_{ad} = 2021$ K (see Table 1). As for the hydrogen flamelet, increasing the strain is observed to suppress NO. In the methane case, however, strain is meanwhile weakening the flame. Indeed, the maximum flame temperature decreases for the methane-air flame as the strain increases, and therefore one can expect, unlike for the hydrogen case, that NO decreases because of the temperature. The further condition of $\varphi = 0.94$ is evaluated for the methane-air flamelet. This value is chosen in this case in order to obtain the same power in output achieved by a premixed hydrogen flame at $\varphi = 0.7$ in a freely propagating configuration, where the power in output P is obtained as the inlet fuel mass flow rate $\dot{m}_f$ multiplied by the fuel lower heating value LHV, $P = \dot{m}_f \cdot LHV$. In this case emissions of NO for the hydrogen flame are even quantitatively lower than those for the methane flame for strain rates $a < 1000$ s^{-1}. For higher strain rates the curves cross each other and the methane flame exhibits the lower emissions instead. As discussed earlier, however, the steeper decrease in the methane-air case is due to the flame becoming inefficient and the consequent decrease of temperature. One can further observe that, for both the equivalence ratios investigated on the methane-air flamelet, NO_x tends to be suppressed more rapidly at high strain as compared to the hydrogen-air flamelet. This indicates that the methane flame is indeed approaching extinction as the strain rate increases.

Further insights on the reasons behind the more ripid decrease of NO in the methane flamelets is provided in Fig. 8b, where the source term of NO across the flamelet at $\varphi = 0.8125$ are plotted for different strain rates. Negative values of $\dot{\omega}_{NO}$ observed around $(x - x_0)/\delta = 0$ are due to the local formation of NO_2 at the relatively low temperatures at this location. Unlike what observed for hydrogen in Section 4.3, the peak of NO source term decreases with strain. Moreover, $\dot{\omega}_{NO}$ also decreases with strain in the further downstream region of the domain, similarly to the hydrogen case. These trends are triggered by the distribution of the main radicals, which follows a similarly decreasing trend, as reported in Section 4 in the supplementary material. It follows that in the case of methane-air combustion the behaviour of the radicals in the tail and downstream of the flame also contributes to the suppression of NO_x but, unlike the hydrogen case, this comes along with a decrease of radicals also in the flame, indicating that the flame is becoming weaker. This explains the steeper decrease with strain of integral NO observed in Fig. 8 for the methane flamelets, since both flame and postflame regions are contributing to the decrease of NO in this case. In the case of hydrogen instead, the combination of its higher reactivity and high diffusivity triggers the strengthening of the flame with strain, which causes a local increase in the main radicals concentration peaks. In turn, this phenomenon contributes to NO formation, and thus limits the overall NO suppression as strain increases, but at the same time allows the flame to sustain much higher strain levels.

4.5. *Effect of pressure*

The effect of increasing pressure on the hydrogen-air flamelet at $\varphi = 0.7$ is investigated in this section. The density-weighted NO integral values are shown in Fig. 9a for the atmospheric condition investigated earlier and the further condition at $p = 5$ bar.

The decrease of NO with strain is observed to be similar for the two pressure conditions, and an almost linear variation is observed in the logarithmic space also for the higher pressure case. Similarly to what observed in Section 4.3, for $p = 5$ bar the peaks of the main radicals mass fraction are observed to increase with strain, and radicals are also suppressed more at downstream positions as strain increases (not shown). Another observation is that the integral of NO mass fraction increases of about one order of magnitude when pressure is increased to 5 bar. The increase of NO_x emissions with pressure has been already observed for hydrogen enriched flames, e.g. de Persis et al. [60], and can be partly attributed to a slight increase of the adiabatic flame temperature. Further insight on the local emissions of NO can be obtained by looking at the

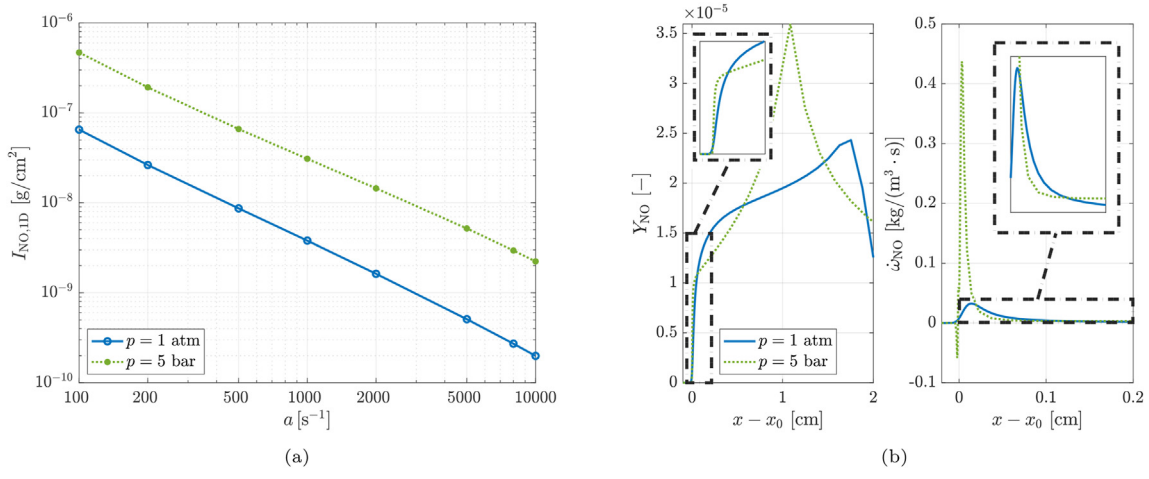

Fig. 9 – (a) Variation of density weighted NO integral I_{NO} with strain a for a hydrogen-air flamelet at $\varphi = 0.7$ at $p = 1$ atm and $p = 5$ bar. (b) Distribution of NO mass fraction Y_{NO} and NO source term $\dot{\omega}_{NO}$ across the flamelets for the two pressure conditions for $a = 500$ s^{-1}. The regions indicated by the dashed rectangle are zoomed out for clarity.

distribution of NO mass fraction and its source term at the two pressure conditions in Fig. 9b. The two flamelets in the figure are compared for a representative strain rate of $a = 500$ s^{-1}. Note that the x-axis is not normalised by the flame thickness in this case since the flame thickness varies with the pressure. A higher peak of source term triggers a steeper local increase in the NO mass fraction at higher pressure as one would expect. However, the flame thickness also decreases by a factor of about five for the higher pressure case, which explains why the source term in the latter case approaches zero more quickly as compared to the atmospheric case. This in turn implies a lower local mass fraction of NO in the higher pressure case downstream of the flame. Nevertheless, moving further downstream, the two curves of the source term for the two pressure conditions intersect again (the reaction rate is again higher for the higher pressure case), which causes a steeper increase of NO mass fraction in the products. This behaviour explains the higher integral values of NO observed in Fig. 9a. Note that the peak of Y_{NO} is located earlier in space in Fig. 9b (left) for the higher pressure case because the consumption speed is decreased by a factor of almost two, and so the flame stabilises closer to the regions of lower flow speed. Still, the integral value of NO is higher because of its stronger source term on the products side.

The above analysis indicates that the behaviour with strain of the hydrogen flame remains qualitatively the same when pressure increases. Additional analyses for further higher pressure were not conducted here due to the uncertainty deriving from the chemical kinetic mechanism to be used, and will be performed in future studies.

4.6. *Effect of equivalence ratio*

The influence of equivalence ratio on the behaviour of NO_x emission with strain is discussed in this section for the hydrogen-air flame. The density-weighted NO integral is plotted as a function of strain for a range of lean equivalence ratios varying from $\varphi = 0.4$ to $\varphi = 0.8$ in Fig. 10a.

In order to assess whether the flame is approaching extinction at the lowest equivalence ratios, the range of strain rates has been extended up to $a = 20000$ s^{-1}. As expected, lower NO values are observed for leaner conditions at the same strain rate due to the lower adiabatic flame temperature. The suppression of NO with strain is confirmed at all the equivalence ratios investigated, but the gradient of this decrease becomes less steep in leaner conditions. This is probably due to the fact that the production of NO via the thermal route, which was observed to be the major contributor for NO suppression with strain, is already lower due to the lower temperatures of the leaner burning regime, and thus strain has a more limited effect in further reducing the NO formation. It is interesting to note that the gradient of decrease of NO with strain is now observed to change significantly for the lower equivalence ratios at the highest strain values. As discussed for the analysis on the methane flame, this indicates that flame extinction conditions are being approached, and it is remarkable that this situation occurs in the hydrogen flame only at very lean regimes ($\varphi = 0.4$) and $a >$ 10000 s^{-1}.

Further insight is provided in the contour plot of Fig. 10b, showing the combined effect of equivalence ratio and strain on the integral NO emissions. The isolines in this figure in particular indicate couples of values (φ, a) for which the integral NO across the flamelet is the same. It can be observed that increasing strain in richer conditions allows to reach outcomes of NO emissions that are comparable to the ones in lean regimes at low strain levels. Considering also that flame extinction is not approached for almost any of the regimes shown in the contour plot, these results indicate that burning hydrogen in potentially unstable, ultra-lean conditions to reduce NO_x emissions may not be necessary as the suppression of NO_x can be compensated by imposing intensive strain rates on the flame.

5. Correlation for the integral NO emissions

A correlation is proposed in this section to estimate the amount of integral NO produced across a flamelet at varying strain rate and equivalence ratio. This correlation is found combining analytical and numerical results, and its derivation is shown next.

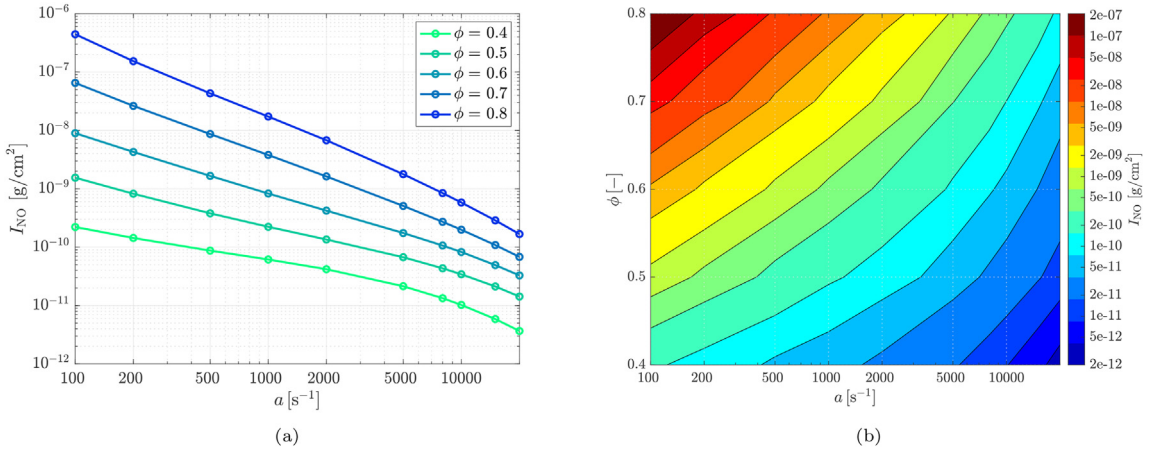

Fig. 10 – (a) Variation of density weighted NO integral I_{NO} with strain a for hydrogen-air flame at different equivalence ratios φ. (b) Contour plot of density weighted NO integral I_{NO} as a function of strain a and equivalence ratio φ.

5.1. *Analytical derivation*

The integral formulation of continuity and NO mass fraction conservation equations in a steady flow reads:

$$\int_A \rho(\mathbf{u}\cdot\mathbf{n})\, dA = 0; \tag{14a}$$

$$\int_A \rho(\mathbf{u}\cdot\mathbf{n})Y_{NO}\, dA = \int_V \dot{\omega}_{NO}\, dV. \tag{14b}$$

where $\mathbf{u}$ is the velocity vector, $\mathbf{n}$ is the unity vector normal to a control volume encompassing the flame and pointing outwards, A is the area of the domain boundary and V is the volume of the integration domain. The source term of NO is here considered to be a mass source term, with dimension [kg/(m^3·s)]. Let's consider a two-dimensional reactants-to-products domain of arbitrary vertical and horizontal dimensions h and L (see Fig. 11a).

Eq. (14b) can be re-arranged as follows:

$$2\int_{-L/2}^{L/2} [\rho u_y Y_{NO}]_{y=\pm h/2} dx = \{\dot{\omega}_{NO}\} x_f h. \tag{15}$$

where x_f is the distance between the flame and the stagnation plane, which without loss of generalities for the present derivation is also assumed to be the region of formation of NO, and $\{\dot{\omega}_{NO}\}$ is the mean value of the NO reaction rate over the same region. The flux of NO across the inlet surfaces is zero consistently to the analysis done in Section 4. The source term of NO has non-zero values only within the flame and in the region between the flame and the stagnation plane as mentioned earlier. The continuity equation can also be re-arranged as follows:

$$-(\rho_r u_{x,r} + \rho_p u_{x,p})h + 2\langle \rho u_y\rangle_{\pm h/2} L = 0, \tag{16}$$

where $\langle \rho u_y\rangle_{\pm h/2}$ refers to the line average along the streamwise direction at $y = \pm h/2$, and the subscripts r and p respectively refer to reactants and products inlet boundaries. It is further assumed that:

$$\int_{-L/2}^{L/2} [\rho u_y Y_{NO}]_{y=\pm h/2} dx \approx \langle u_y\rangle \int_{-L/2}^{L/2} [\rho Y_{NO}]_{y=\pm h/2} dx, \tag{17a}$$

$$\langle \rho u_y\rangle \approx \langle\rho\rangle\langle u_y\rangle, \tag{17b}$$

where all the averages indicated by the $\langle\cdot\rangle$ operator are evaluated along the streamwise direction at $y = \pm h/2$, and the subscript $\pm h/2$ is omitted from now on for clarity of notation. The above approximations were verified *a posteriori* using the two-dimensional simulations data and observed to remain accurate for the range of conditions explored in this study. By substituting Eq. (17b) into Eq. (16) one obtains:

$$\langle u_y\rangle = \frac{\rho_r u_{x,r} + \rho_p u_{x,p}}{2\langle\rho\rangle}\frac{h}{L}. \tag{18}$$

By substituting equations (17a) and (18) into Eq. (15), the following expression is thus found:

$$\frac{\rho_r u_{x,r} + \rho_p u_{x,p}}{\langle\rho\rangle L}\int_{-L/2}^{L/2} [\rho Y_{NO}]_{y=\pm h/2} dx = \{\dot{\omega}_{NO}\} x_f. \tag{19}$$

where the vertical dimension h cancels out, indicating that this expression is independent of the vertical direction. This finding is consistent with the discussion in Section 4.1, and particularly Eq. (9), where the 1D density weighted integral of NO was found to be substantially independent on the vertical direction in the two-dimensional simulations performed. The integral on the left-hand-side of Eq. (19) is by definition the density weighted NO integral I_{NO} evaluated across one-dimensional flamelets in this study, whose prediction is the

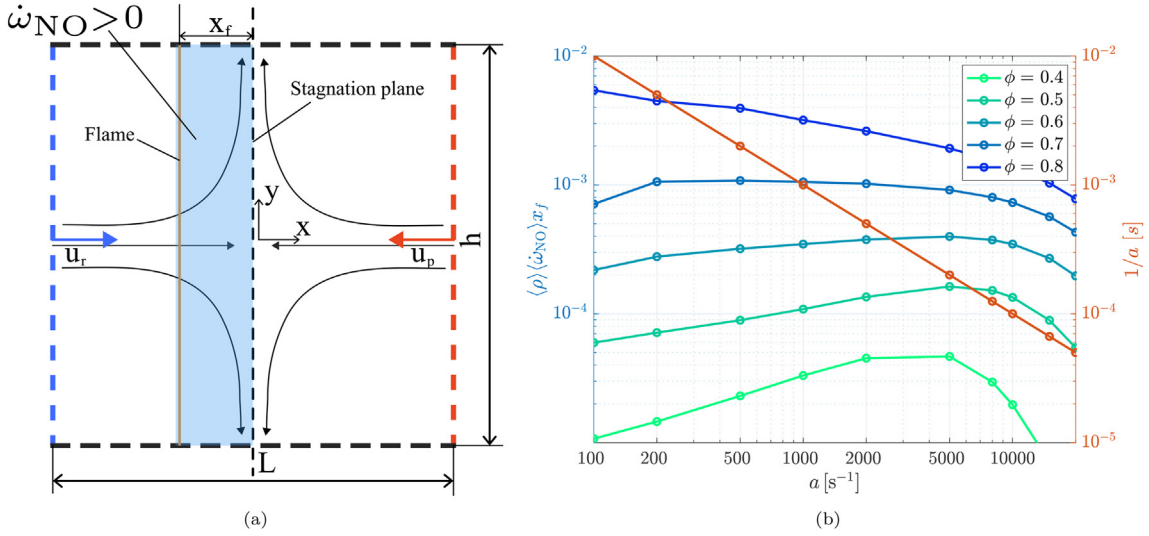

Fig. 11 – (a) Control volume around the counter-flow premixed reactants-to-products flame configuration used for the analytical derivation of the correlation for I_{NO}. (b) Variation with strain a of the numerator of Eq. (24) for the hydrogen-air premixed flame at different equivalence ratios φ, as compared to the function $1/a$.

objective of the present derivation. From Eq. (19), I_{NO} can thus be expressed as:

$$I_{NO} = \frac{\langle\rho\rangle\{\dot{\omega}_{NO}\}x_f L}{\rho_r u_{x,r} + \rho_p u_{x,p}}. \tag{20}$$

As discussed in Section 3.1, in the investigated counter-flow flamelet setup the stagnation plane is always located at $x = 0$. The applied strain rate is thus

$$a = -\left(\frac{du_x}{dx}\right)_p = \frac{u_p}{L/2}. \tag{21}$$

Furthermore, Darabiha et al. [35] have shown that for the type of flows in the present configuration the following relation between reactants and products inlet velocities can be derived:

$$\rho_p u_{x,p}^2 = \rho_r u_{x,r}^2. \tag{22}$$

Combining equations (21) and (22), $u_{x,p}$ and $u_{x,r}$ can be expressed as a function of the applied strain rate:

$$u_{x,p} = \frac{a}{L/2}; \tag{23a}$$

$$u_{x,r} = u_{x,p}\sqrt{\frac{\rho_p}{\rho_r}} = \frac{a}{L/2}\sqrt{\frac{\rho_p}{\rho_r}}. \tag{23b}$$

By substituting these relations into Eq. (20), one obtains:

$$I_{NO} = \frac{\langle\rho\rangle\{\dot{\omega}_{NO}\}x_f L}{\frac{1}{2}aL\left(\rho_r\sqrt{\frac{\rho_p}{\rho_r}} + \rho_p\right)} = \frac{2\langle\rho\rangle\{\dot{\omega}_{NO}\}x_f}{a\left(\sqrt{\rho_p\rho_r} + \rho_p\right)}. \tag{24}$$

This relation shows the dependence of I_{NO} on $1/a$ and is consistent with the findings obtained from the simulations presented in Section 4. On the other hand, the numerator in Eq. (24) also is influenced by strain through x_f, because different consumption speeds of the flame at different strain rates imply different flame stabilisation points. The average source term of NO can also be expected to vary with strain, which one might deduce from Fig. 6f, and similar considerations hold for the averaged density. In order to understand this dependence and the relative contribution on I_{NO} of numerator and denumerator in Eq. (24) as strain increases, the latter two are calculated using the simulations data for the hydrogen-air counter-flow flamelets at different equivalence ratios, and shown in Fig. 11b. It can be seen that $1/a$ is a steeper function of strain than $\langle\rho\rangle\langle\dot{\omega}_{NO}\rangle x_f$. The numerator of Eq. (24) has a stronger dependence on strain only for the leanest condition of $\varphi = 0.4$, and therefore at intermediate lean equivalence ratios and moderate-high strains one could conclude that I_{NO} has an almost linear dependence on $1/a$. Nevertheless, in order to quantify the effect of the numerator, particularly for the more extreme conditions of equivalence ratio and strain, a semi-empirical approach is employed, which is described next.

5.2. *Semi-empirical estimation of* I_{NO}

In the one-dimensional reactants-to-products counter-flow hydrogen flamelets investigated in this study, the combined influence of equivalence ratio and strain on the density weighted NO integral are observed to closely follow the following correlation function

$$I_{NO}(a,\varphi) = \int_{-L/2}^{L/2} \rho Y_{NO} dx = k(\varphi)\cdot a^{l(\varphi)} \tag{25}$$

where the coefficients k and l are respectively an exponential and a linear function of φ:

$$k(\varphi) = k_1 \cdot e^{k_2\varphi} \tag{26a}$$

$$l(\varphi) = l_1\varphi + l_2 \tag{26b}$$

The coefficients k_1, k_2, l_1 and l_2 are reported in Table 6.

For the range of equivalence ratios investigated, the coefficient l is always negative, enabling I_{NO} to be a decreasing function of strain. Furthermore, the value of l is found to be about $l \approx -1$, implying that the NO integral function behaves almost as a decreasing hyperbolic function of strain:

$$I_{NO}(a) \sim \frac{1}{a}. \tag{27}$$

which is consistent with the analytical findings in Section 5.1.

In Fig. 12a the values for I_{NO} obtained from the correlation of Eq. (25) using the best fit values of Table 6 are compared to those computed from the hydrogen-air premixed counter-flow flamelets. The correlation error is also reported in the contour plot in Fig. 12b.

Higher errors are observed only for very high strain and very lean conditions, where extinction might start to be approached and thus the I_{NO} curve with strain starts to depart from a quasi-linear behaviour in the logarithmic space. For all other conditions where the regime is far from extinction, the error is below 10%. It is worth noting that a similar correlation for I_{NO} could be used for methane flames k and l. However, in this case the relation would hold for only a limited region of the domain shown in Fig. 12b, since the methane flamelet approaches extinction much more easily than the hydrogen flame. The strong reactivity of the hydrogen flame allows instead for the correlation presented here to hold for a wide range of strains and equivalence ratios. The correlation in Eq. (25) can thus be used to quickly assess in preliminary analyses how the integral NO emissions vary in lean premixed hydrogen flames with strain rate and equivalence ratio, and eventually aid the design of novel combustion systems where NO_x is suppressed by their combined effect. On the other hand, how to stabilise the hydrogen flame under intensive strain conditions and how the high turbulence levels in practical combustor systems

Table 6 – Fitting values for the coefficients in the correlation of Eq. (25).

Coefficient	value	dimension
k_1	$5.413 \cdot 10^{-14}$	$g/(s \cdot cm^2)$
k_2	28.22	–
l_1	−2.036	–
l_2	0.1769	–

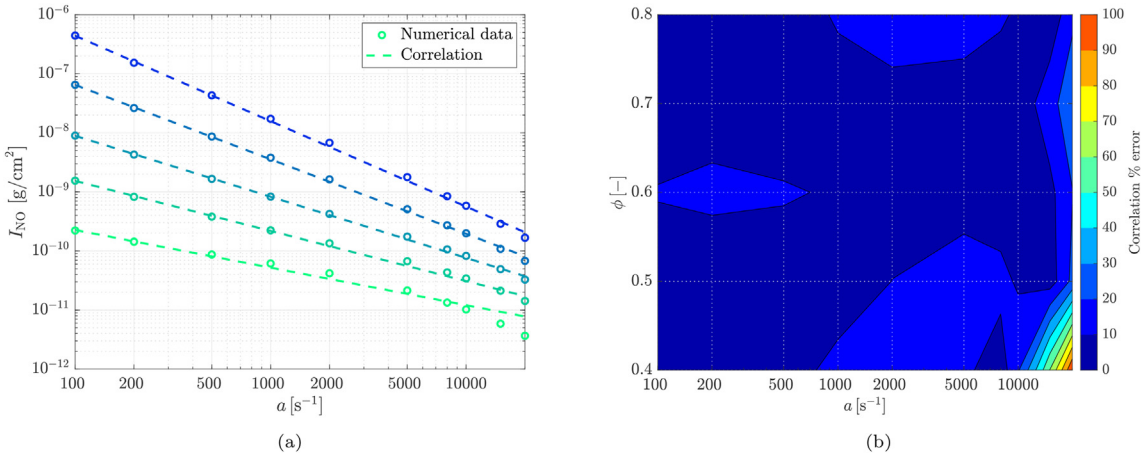

Fig. 12 – (a) Comparison of integral NO I_{NO} with strain obtained from numerical simulations of premixed hydrogen-air flamelets in counter-flow at different equivalence ratios φ, and the correlation expression of Eq. (25). (b) Contour plot of the correlation error with respect to numerical data.

would affect the outcomes presented here, is still an open question, and insights on this will be provided in future studies.

6. Conclusions

Detailed chemistry analyses have been conducted on pure hydrogen-air lean premixed and strained flamelets in a counter-flow reactants-to-products configuration. The study investigated a broad range of strain rates, including very high levels rarely considered before in the literature. The main findings are summarised below.

- NO_x is significantly suppressed as the strain rate increases, despite the hydrogen flame becoming more reactive. This is shown for the first time for pure hydrogen fuel and lean flames.
- The NO_x suppression is not a consequence of any numerical setup preconditioning or resident time effect.
- The most substantial decrease of NO_x with strain is observed across the thermal pathway due to the local redistribution of radicals, even though the temperature across the flame does not decrease with strain.
- The impact of high strain effects has also been studied at higher pressure and for methane fuel, showing generally similar trends in NO_x suppression, although with different rates of decrease due to an occasionally different radical redistribution mechanism.
- The analysis of multiple lean equivalence ratios further indicates that in place of ultra-lean hydrogen flames, richer mixtures under high strain can result in the same NO_x suppression.

Finally, a correlation for the prediction of the density-weighted integral of NO as a function of strain and equivalence ratio has been derived for premixed counter-flow hydrogen flames, where the integral value of NO is found to have an almost-linear dependence with the reciprocal of the applied strain rate. This correlation can be used for preliminary analyses oriented to the design of low-NO_x, novel combustion systems that can employ a combination of lean flames and high strain. Nevertheless, flame stability and emissions at highly turbulent, practical conditions, may result in different behaviours than those observed for laminar flames in the current study, and therefore further investigations are necessary. These investigations will be presented in future studies.

Declaration of competing interest

The authors declare that they have no known competing financial interests or personal relationships that could have appeared to influence the work reported in this paper.

Acknowledgments

A. Porcarelli and I. Langella acknowledge the Dutch Ministry of Education and Science for providing funding support to this project via the Sector Plan scheme. B. Kruljević and I. Langella further acknowledge support from the Engineering and Physical Sciences Research Council, grant no. EP/T028084/1.

Appendix A. Supplementary data

Supplementary data to this article can be found online at https://doi.org/10.1016/j.ijhydene.2023.08.110.

REFERENCES

[1] Birol F. World energy outlook. 2018. https://www.iea.org/reports/world-energy-outlook-2018/renewables. [Accessed 12 July 2023].

[2] Masri AR. Challenges for turbulent combustion. Proc Combust Inst 2021;38:121–55. https://doi.org/10.1016/j.proci.2020.07.144.
[3] Turner JA. Sustainable hydrogen production. Science 2004;305:972–4. https://doi.org/10.1126/science.1103197.
[4] Jensen SH, Larsen PH, Mogensen M. Hydrogen and synthetic fuel production from renewable energy sources. Int J Hydrogen Energy 2007;32:3253–7. https://doi.org/10.1016/j.ijhydene.2007.04.042.
[5] Lehner M, Tichler R, Steinmüller H, Koppe M, Methanation. Power-to-Gas: technology and business models. Springer Int Publ; 2014. p. 41–61.
[6] Malins C. What role is there for electrofuel technologies in european transport's low carbon future?. https://www.transportenvironment.org/discover/role-electrofuel-technologies-europes-low-carbon-transport-future/. [Accessed 12 July 2023].
[7] Tornatore C, Marchitto L, Sabia P, De Joannon M. Ammonia as green fuel in internal combustion engines: state-of-the-art and future perspectives. Front Mech Eng 2022:72. https://doi.org/10.3389/fmech.2022.944201.
[8] Singla MK, Nijhawan P, Oberoi AS. Hydrogen fuel and fuel cell technology for cleaner future: a review. Environ Sci Pollut Res 2021;28:15607–26. https://doi.org/10.1007/s11356-020-12231-8.
[9] White C, Steeper R, Lutz A. The hydrogen-fueled internal combustion engine: a technical review. Int J Hydrogen Energy 2006;31:1292–305. https://doi.org/10.1016/j.ijhydene.2005.12.001.
[10] Jackson GS, Sai R, Plaia JM, Boggs CM, Kiger KT. Influence of h2 on the response of lean premixed ch4 flames to high strained flows. Combust Flame 2003;132:503–11. https://doi.org/10.1016/S0010-2180(02)00496-0.
[11] Cho E-S, Chung SH. Improvement of flame stability and nox reduction in hydrogen-added ultra lean premixed combustion. J Mech Sci Technol 2009;23:650–8. https://doi.org/10.1007/s12206-008-1223-x.
[12] Barbosa S, Garcia MdLC, Ducruix S, Labegorre B, Lacas F. Control of combustion instabilities by local injection of hydrogen. Proc Combust Inst 2007;31:3207–14. https://doi.org/10.1016/j.proci.2006.07.085.
[13] Lipatnikov A, Chomiak J. Molecular transport effects on turbulent flame propagation and structure. Prog Energy Combust Sci 2005;31:1–73. https://doi.org/10.1016/j.pecs.2004.07.001.
[14] Huang Y, Yang V. Dynamics and stability of lean-premixed swirl-stabilized combustion. Prog Energy Combust Sci 2009;35:293–364. https://doi.org/10.1016/j.pecs.2009.01.002.
[15] Ducruix S, Schuller T, Durox D, Candel S. Combustion dynamics and instabilities: elementary coupling and driving mechanisms. J Propul Power 2003;19:722–34. https://doi.org/10.2514/2.6182.
[16] Speth RL, Ghoniem AF. Using a strained flame model to collapse dynamic mode data in a swirl-stabilized syngas combustor. Proc Combust Inst 2009;32:2993–3000. https://doi.org/10.1016/j.proci.2008.05.072.
[17] Hu Y, Kurose R. Large-eddy simulation of turbulent autoigniting hydrogen lifted jet flame with a multi-regime flamelet approach. Int J Hydrogen Energy 2019;44:6313–24. https://doi.org/10.1016/j.ijhydene.2019.01.096.
[18] Johannessen B, North A, Dibble R, Løvås T. Experimental studies of autoignition events in unsteady hydrogen–air flames. Combust Flame 2015;162:3210–9. https://doi.org/10.1016/j.combustflame.2015.05.008.
[19] Dinesh KR, Shalaby H, Luo K, Van Oijen J, Thévenin D. High hydrogen content syngas fuel burning in lean premixed spherical flames at elevated pressures: effects of preferential diffusion. Int J Hydrogen Energy 2016;41:18231–49. https://doi.org/10.1016/j.ijhydene.2016.07.086.
[20] Abbasi-Atibeh E, Bergthorson JM. Differential diffusion effects in counter-flow premixed hydrogen-enriched methane and propane flames. Proc Combust Inst 2019;37:2399–406. https://doi.org/10.1016/J.PROCI.2018.08.006.
[21] Vance FH, Shoshin Y, de Goey L, van Oijen JA. Quantifying the impact of heat loss, stretch and preferential diffusion effects to the anchoring of bluff body stabilized premixed flames. Combust Flame 2022;237:111729. https://doi.org/10.1016/j.combustflame.2021.111729.
[22] Ashurst WT, Peters N, Smooke M. Numerical simulation of turbulent flame structure with non-unity lewis number. Combust Sci Technol 1987;53:339–75. https://doi.org/10.1080/00102208708947036.
[23] Haworth D, Poinsot T. Numerical simulations of lewis number effects in turbulent premixed flames. J Fluid Mech 1992;244:405–36. https://doi.org/10.1017/S0022112092003124.
[24] Baum M, Poinsot T, Haworth D, Darabiha N. Direct numerical simulation of h2/o2/n2 flames with complex chemistry in two-dimensional turbulent flows. J Fluid Mech 1994;281:1–32. https://doi.org/10.1017/S0022112094003010.
[25] Van Oijen J, Donini A, Bastiaans R, ten Thije Boonkkamp J, De Goey L. State-of-the-art in premixed combustion modeling using flamelet generated manifolds. Prog Energy Combust Sci 2016;57:30–74. https://doi.org/10.1016/j.pecs.2016.07.001.
[26] Marzouk YM, Speth RL, Ghoniem AF. Combined effects of curvature and strain on hydrogen enriched lean methane flames. Technical Report. Livermore, CA (United States): Sandia National Lab.(SNL-CA); 2005. URL: https://www.osti.gov/servlets/purl/1465582. [Accessed 13 July 2023].
[27] Ning D, Fan A, Yao H. Effects of fuel composition and strain rate on no emission of premixed counter-flow h2/co/air flames. Int J Hydrogen Energy 2017;42:10466–74. https://doi.org/10.1016/j.ijhydene.2016.12.059.
[28] Liang W, Wu F, Law CK. Extrapolation of laminar flame speeds from stretched flames: role of finite flame thickness. Proc Combust Inst 2017;36:1137–43. https://doi.org/10.1016/J.PROCI.2016.08.074.
[29] Varea E, Beeckmann J, Pitsch H, Chen Z, Renou B. Determination of burning velocities from spherically expanding h2/air flames. Proc Combust Inst 2015;35:711–9. https://doi.org/10.1016/j.proci.2014.05.137.
[30] Xie TF, Wang PY. Analysis of no formation in counterflow premixed hydrogen-air flame. In: Applied mechanics and materials, vol. 284. Trans Tech Publ; 2013. p. 601–7. https://doi.org/10.4028/www.scientific.net/AMM.284-287.601.
[31] Nilsson P, Bai X-S. Effects of flame stretch and wrinkling on co formation in turbulent premixed combustion. Proc Combust Inst 2002;29:1873–9. https://doi.org/10.1016/S1540-7489(02)80227-9.
[32] Hawkes ER, Chen JH. Comparison of direct numerical simulation of lean premixed methane–air flames with strained laminar flame calculations. Combust Flame 2006;144:112–25. https://doi.org/10.1016/j.combustflame.2005.07.002.
[33] Polifke W, Flohr P, Brandt M. Modeling of inhomogeneously premixed combustion with an extended tfc model. J Eng Gas Turbines Power 2002;124:58–65. https://doi.org/10.1115/1.1394964.
[34] Libby PA, Williams FA. Structure of laminar flamelets in premixed turbulent flames. Combust Flame 1982;44:287–303. https://doi.org/10.1016/0010-2180(82)90079-7.
[35] Darabiha N, Candel S, Marble F. The effect of strain rate on a premixed laminar flame. Combust Flame 1986;64:203–17. https://doi.org/10.1016/0010-2180(86)90057-X.

[36] Kolla H, Swaminathan N. Strained flamelets for turbulent premixed flames, i: formulation and planar flame results. Combust Flame 2010;157:943–54. https://doi.org/10.1016/j.combustflame.2010.01.018.
[37] Langella I, Swaminathan N. Unstrained and strained flamelets for les of premixed combustion. Combust Theor Model 2016;20:410–40. https://doi.org/10.1080/13647830.2016.1140230.
[38] Weller HG, Tabor G, Jasak H, Fureby C. A tensorial approach to computational continuum mechanics using object-oriented techniques. Comput Phys 1998;12:620–31. https://doi.org/10.1063/1.168744.
[39] Poinsot T, Veynante D. Theoretical and numerical combustion. RT Edwards, Inc.; 2005.
[40] Poling BE, Prausnitz JM, O'connell JP. Properties of gases and liquids. McGraw-Hill Educ; 2001. URL: https://www.accessengineeringlibrary.com/content/book/9780070116825.
[41] Chapman S, Cowling TG. The mathematical theory of non-uniform gases: an account of the kinetic theory of viscosity, thermal conduction and diffusion in gases. Cambridge Univ press; 1990.
[42] Novaresio V, García-Camprubí M, Izquierdo S, Asinari P, Fueyo N. An open-source library for the numerical modeling of mass-transfer in solid oxide fuel cells. Comput Phys Commun 2012;183:125–46. https://doi.org/10.1016/j.cpc.2011.08.003.
[43] Smith G, et al. Gri-mech 3.0. 2000. http://combustion.berkeley.edu/gri-mech/version30/text30.html. [Accessed 12 July 2023].
[44] Jaravel T, Riber E, Cuenot B, Pepiot P. Prediction of flame structure and pollutant formation of sandia flame d using large eddy simulation with direct integration of chemical kinetics. Combust Flame 2018;188:180–98. https://doi.org/10.1016/j.combustflame.2017.08.028.
[45] Cazeres Q. Analysis and reduction of chemical kinetics for combustion applications. Ph.D. thesis. Toulouse: INPT; 2021. URL: https://oatao.univ-toulouse.fr/28503/.
[46] Konnov A. Implementation of the ncn pathway of prompt-no formation in the detailed reaction mechanism. Combust Flame 2009;156:2093–105. https://doi.org/10.1016/j.combustflame.2009.03.016.
[47] Lamoureux N, Desgroux P, El Bakali A, Pauwels J-F. Experimental and numerical study of the role of ncn in prompt-no formation in low-pressure ch4–o2–n2 and c2h2–o2–n2 flames. Combust Flame 2010;157:1929–41. https://doi.org/10.1016/j.combustflame.2010.03.013.
[48] Contino F, Jeanmart H, Lucchini T, D'Errico G. Coupling of in situ adaptive tabulation and dynamic adaptive chemistry: an effective method for solving combustion in engine simulations. Proc Combust Inst 2011;33:3057–64. https://doi.org/10.1016/J.PROCI.2010.08.002.
[49] Eindhoven University of Technology, CHEM1D. A one dimensional laminar flame code. 2021.
[50] Ramaekers W. Development of flamelet generated manifolds for partially-premixed flame simulations. Ph.D. thesis. Technische Universiteit Eindhoven; 2011. https://doi.org/10.6100/IR716707.
[51] Somers B. The simulation of flat flames with detailed and reduced chemical models. Gastec NV NL: Ph.D. thesis; 1994. https://doi.org/10.6100/IR420430.
[52] Rogg B. Response and flamelet structure of stretched premixed methane-air flames. Combust Flame 1988;73:45–65. https://doi.org/10.1016/0010-2180(88)90052-1.
[53] Zirwes T, Zhang F, Habisreuther P, Hansinger M, Bockhorn H, Pfitzner M, Trimis D. Quasi-dns dataset of a piloted flame with inhomogeneous inlet conditions. Flow, Turbul Combust 2020;104:997–1027. https://doi.org/10.1007/s10494-019-00081-5.
[54] Cazères Q, Pepiot P, Riber E, Cuenot B. A fully automatic procedure for the analytical reduction of chemical kinetics mechanisms for computational fluid dynamics applications. Fuel 2021;303:121247. https://doi.org/10.1016/j.fuel.2021.121247.
[55] Capurso T, Laera D, Riber E, Cuenot B. Nox pathways in lean partially premixed swirling h2-air turbulent flame. Combust Flame 2023;248:112581. https://doi.org/10.1016/J.COMBUSTFLAME.2022.112581.
[56] Kee RJ, Rupley FM, Miller JA. Chemkin-II: a Fortran chemical kinetics package for the analysis of gas-phase chemical kinetics. Technical Report. Livermore, CA (United States): Sandia National Lab.(SNL-CA); 1989. https://doi.org/10.2172/5681118. URL: https://www.osti.gov/biblio/5681118.
[57] Rørtveit GJ, Hustad JE, Li S-C, Williams FA. Effects of diluents on nox formation in hydrogen counterflow flames. Combust Flame 2002;130:48–61. https://doi.org/10.1016/S0010-2180(02)00362-0.
[58] Samiran NA, Chong CT, Ng J-H, Tran M-V, Ong HC, Valera-Medina A, Chong WWF, Jaafar MNM. Experimental and numerical studies on the premixed syngas swirl flames in a model combustor. Int J Hydrogen Energy 2019;44:24126–39. https://doi.org/10.1016/J.IJHYDENE.2019.07.158.
[59] Williams TC, Shaddix* CR, Schefer RW. Effect of syngas composition and co2-diluted oxygen on performance of a premixed swirl-stabilized combustor. Combust Sci Technol 2007;180:64–88. https://doi.org/10.1080/00102200701487061.
[60] de Persis S, Idir M, Molet J, Pillier L. Effect of hydrogen addition on nox formation in high-pressure counter-flow premixed ch4/air flames. Int J Hydrogen Energy 2019;44:23484–502. https://doi.org/10.1016/j.ijhydene.2019.07.002.